National Technical
University of Athens

School of Applied
Mathematical
and Physics Science

School of Mechanical
Engineering

N.C.S.R. "Demokritos"

Inst. of Nanoscience
and Nanotechnology

Inst. of Nuclear and
Particle Physics

Interdepartmental Master's Science Degree in Physics
"Physics & Technological Applications"

Differential Cross-Section Measurements of the $^{18}O(p,\alpha_0)^{15}N$ Reaction for NRA Purposes

MASTER THESIS
by Anastasia Kotsovolou

Supervisor: *Dr Anastasios Lagoyannis, Director of Research*
INPP, NCSR "Demokritos"

Athens, July 2024

ΕΘΝΙΚΟ ΜΕΤΣΟΒΙΟ
ΠΟΛΥΤΕΧΝΕΙΟ

ΣΧΟΛΗ ΕΦΑΡΜΟΣΜΕΝΩΝ
ΜΑΘΗΜΑΤΙΚΩΝ
ΚΑΙ ΦΥΣΙΚΩΝ ΕΠΙΣΤΗΜΩΝ

ΣΧΟΛΗ ΜΗΧΑΝΟΛΟΓΩΝ
ΜΗΧΑΝΙΚΩΝ

ΕΚΕΦΕ «ΔΗΜΟΚΡΙΤΟΣ»

ΙΝΣΤΙΤΟΥΤΟ ΝΑΝΟΕΠΙΣΤΗΜΗΣ
ΚΑΙ ΝΑΝΟΤΕΧΝΟΛΟΓΙΑΣ

ΙΝΣΤΙΤΟΥΤΟ ΠΥΡΗΝΙΚΗΣ ΚΑΙ
ΣΩΜΑΤΙΔΙΑΚΗΣ ΦΥΣΙΚΗΣ

Διατμηματικό Πρόγραμμα Μεταπτυχιακών Σπουδών
«Φυσική και Τεχνολογικές Εφαρμογές»

Μετρήσεις Διαφορικής Ενεργού Διατομής της Αντίδρασης $^{18}\mathbf{O}(\mathbf{p},\alpha_0)^{15}\mathbf{N}$

ΜΕΤΑΠΤΥΧΙΑΚΗ ΔΙΠΛΩΜΑΤΙΚΗ ΕΡΓΑΣΙΑ

της Αναστασίας Κωτσόβολου

Επιβλέπων: Δρ. Αναστάσιος Λαγογιάννης, Διευθυντής Ερευνών
ΙΠΣΦ, ΕΚΕΦΕ "Δημόκριτος"

Αθήνα, Ιούλιος 2024

National Technical
University of Athens

School of Applied
Mathematical
and Physics Science

School of Mechanical
Engineering

N.C.S.R. "Demokritos"

Inst. of Nanoscience
and Nanotechnology

Inst. of Nuclear and
Particle Physics

Differential Cross-Section Measurements of the $^{18}\mathrm{O}(\mathrm{p},\alpha_0)^{15}\mathrm{N}$ Reaction for NRA Purposes

Anastasia Kotsovolou

Master's Thesis Committee
Michail Axiotis, Senior Researcher
Anastasios Lagoyannis, Director of Research
& Theo Mertzimekis, Associate Professor

Athens, July 2024

Acknowledgements

This thesis would not have been completed without the help and support of several people to whom I owe my gratitude. I could not have undertaken this journey without my supervisor, Director of Research, Anastasios Lagoyannis, whose mentorship was invaluable to me at every level. I also extend my gratitude to Researcher Michail Axioti, a constant presence in our lab, always available and willing to offer his help. I cannot forget Prof. Mike Kokkori for the hours he dedicated and the knowledge he shared with me. Special thanks to Associate Prof. Theo Mertzimekis, who, although did not participate in the experiment, has continuously supported me since my first steps in the field.

I am also thankful to all the personnel in the Tandem lab for creating a great and friendly working environment, especially Miltiadis Andrianis and Angelos Laoutaris, who provided the beam. Thanks should also go to the NTUA nuclear physics group for the knowledge I gained from their projects and their help with mine, especially Anastasia, Evangelia, and Anna.

Many thanks to all of the above; the night shifts of the experiment would not have been possible without their help.

I would also like to mention Assistant Prof. Mary Diakaki, who managed to find the paper written by Amsel in 1964, allowing me to address the discrepancies with IBANDL.

Lastly, many thanks to my friend Christina for her support, especially during the writing of this thesis.

Contents

Abstract

This study aims at the investigation of ^{18}O, focusing on the differential cross-section measurements of the $^{18}O(p,\alpha_0)^{15}N$ reaction, conducted within the proton beam energy range of 1-2 MeV, suitable for stable isotopic tracing and concentration depth profiling in the framework of the NRA (Nuclear Reaction Analysis) technique. The measurements were carried out with a variable energy step of either 10 or 20 keV. Two distinct backscattering detection angles were examined, specifically 170^o and 160^o, using 500 μm thick Surface-Barrier (SSB) detectors. The proton beam source for these experiments was provided by the recently refurbished HV TN-11 5.5 MV Tandem Accelerator located at the National Center for Scientific Research "Demokritos" in Athens, Greece.

The experimental target employed in this study consisted of a thin layer of $T\alpha_2O_5$ highly enriched in ^{18}O, which was produced on the surface of a thick tantalum foil via anodization. The thickness of the oxygen layer was initially provided by the manufacturer but was also independently measured using the $^{18}O(d,\alpha)$ reaction. Given the thickness of the target, both a chopper and SIMNRA simulations were employed to determine the $Q \cdot \Omega$ product.

The differential cross-section values were determined using the absolute measurement technique. The final results yielded higher values compared to the existing literature. Some of the observed discrepancies were attributed to inaccuracies in the corresponding database entries.

Περίληψη

Αυτή η εργασία στοχεύει στη μελέτη του ισοτόπου του οξυγόνου ^{18}O, εστιάζοντας στις μετρήσεις της διαφορικής ενεργού διατομής της αντίδρασης $^{18}O(p,\alpha_0)^{15}N$, καλύπτοντας ενεργειακό εύρος δέσμης 1-2 MeV. Είναι κατάλληλη για ανίχνευση σταθερών ισοτόπων και προφιλομετρία συγκέντρωσης του ισοτόπου σε βάθος στα πλαίσια της τεχνικής NRA (Nuclear Reaction Analysis). Οι μετρήσεις ακολούθησαν ενεργειακό βήμα των 10 ή 20 keV ανάλογα με το ρυθμό μετα- βολής της διαφορικής ενεργού διατομής. Εξετάστηκαν δύο γωνίες οπισθοσκέδασης, και συγκεκριμένα τοποθετήθηκαν ανιχνευτές πυριτίου SSB των 500μm στις 170° και 160°. Τη δέσμη πρωτονίων για τις πειραματικές μετρήσεις παρείχε ο προσφάτως ανακαινισμένος HV TN-11 5.5 MV Tandem επιταχυντής που βρίσκεται στον Εθνικό Κέντρο Έρευνας Φυσικών Επιστημών "Δημόκριτος" στην Αθήνα.

Ο στόχος που χρησιμοποιήθηκε για αυτή τη μελέτη αποτελείται από ένα λεπτό στρώμα Ta_2O_5, εμπλουτισμένο με ^{18}O, που δημιουργήθηκε πάνω σε παχύ στρώμα ταντάλου με την τεχνική της ανοδίωσης. Το πάχος του στόχου παρέχεται από τον κατασκευαστή, αλλά επίσης υπολογίστηκε ανεξάρτητα χρησιμοποιώντας την αντίδραση $^{18}O(d,\alpha)^{16}N$. Δεδομένου του πάχους του στόχου, χρησιμοποιήθηκε chopper και προσομοιώσεις SIMNRA για τον καθορισμό του μεγέθους $Q\cdot\Omega$.

Οι τιμές της διαφορικής ενεργού διατομής υπολογίστηκαν χρησιμοποιώντας την τεχνική της απόλυτης μέτρησης. Τα τελικά αποτελέσματα εμφάνισαν σταθερά λίγο υψηλότερες τιμές, σε σύγκριση με την υπάρχουσα βιβλιογραφία. Κάποιες από τις παρατηρούμενες ασυμφωνίες δεδομένων αποδόθηκαν σε εσφαλμένες τιμές των αντίστοιχων βάσεων δεδομένων.

Introduction

Oxygen is Earth's most abundant element, and after hydrogen and helium, it is also the third-most abundant element in the universe. Diatomic oxygen gas currently constitutes 20.95% of the Earth's atmosphere, while oxygen makes up almost half of the Earth's crust in the form of oxides.[1] As it is a highly reactive element, it finds various applications in the semiconductor industry, biological systems, transport processes in thin films, solid-state electrochemistry, and even metallurgy. It is comprised of three natural stable isotopes, namely $^{16}O(99.76\%)$, $^{17}O(0.04\%)$, and $^{18}O(0.2\%)$. The predominance of ^{16}O, along with the high abundance of natural oxygen in nature, renders ^{18}O particularly valuable for stable isotopic tracing purposes, especially when the diffusion or deep penetration of oxygen in material surfaces needs to be carefully quantified. This procedure can be best monitored using oxygen gas or compounds highly enriched in ^{18}O.

In the investigation of (p,α) reactions involving ^{18}O and ^{16}O, it is also observed that the former exhibits elevated Q-values and greater cross sections, while the latter manifests a negative Q-value. [2], [3] Moreover, determining the cross-section of the $^{18}O(p,\alpha_0)$ reaction is crucial, as it influences the rate of hydrogen burning of ^{18}O in the CNO cycle in astrophysics [4]. In solid-state physics, it is connected with surface oxidation and oxygen diffusion in solids. It is obvious, that all these applications require reliable differential and consequently total cross-section datasets within the experimental data libraries.

It swiftly became evident that the more effective approaches for the depth profiling of oxygen involve secondary ion mass spectrometry (SIMS) and nuclear reaction analysis (NRA). SIMS, a sputter-based analytical technique, poses challenges due to its preferential sputtering, especially for elements with significantly different mass numbers, such as metal oxides or metal hydrides. For this method, it is necessary to use a reference material as close to the one under study as possible or to extrapolate to infinite velocity from the secondary ion energy spectra. NRA, based on nuclear reactions, does not need a reference material and is non-destructive. $^{18}O(p,a_0)$ reaction was among the very first to be studied historically and the pioneer measurement carried out by G. Amsel in 1964 [5] set the ground for the further development and evolution of NRA and all the other related IBA techniques.

It is noteworthy that this is the only available measurement for the 1-2 MeV energy range and this angle, whereas the reaction has been extensively studied at lower energies due to its astrophysical significance. Thus, this study aims to evaluate the existing data and contribute to the expansion of theoretically evaluated datasets obtained via the online SigmaCalc code, while also providing data for additional detection angles.

Chapter 1

Theoretical Background

1.1 Fundamental concepts

This thesis aims to study differential cross-sections, which is the key to certain depth profiling ion beam analysis techniques. These techniques are based on nuclear reactions, namely the interaction between two nuclei resulting in the emission of other light nuclei or/and gamma radiation. The reaction products are detected providing information about the investigated sample.

1.1.1 Differential cross section

Cross-section is a necessary quantity for ion beam analysis techniques, giving a measure of the probability for a nuclear reaction to occur. [8] It can be analytically calculated using the Rutherford formula 1.1, which denotes the probability of a particle (Z_1, M_1) with energy E to be scattered from a nucleus (Z_2, M_2) in the laboratory system.

$$\sigma_R(E,\theta) = \left(\frac{Z_1 Z_2 e^2}{4E}\right)^2 \frac{4[(M_2{}^2 - M_1{}^2 sin^2\theta)^{1/2} + M_2 cos\theta]^2}{M_2 sin^4\theta (M_2{}^2 - M_1{}^2 sin^2\theta)^{1/2}} \tag{1.1}$$

Unfortunately, Rutherford's cross-section formula applies only to specific cases, usually when light ions (e.g. protons) collide with heavy elements. When those conditions are not met, cross-section can not be calculated analytically and global libraries with experimental cross-section values are used instead. Each value corresponds to a specific reaction, and as there are still reactions with no experimental data, those libraries are constantly updated.

The experimental cross-section values are calculated following equation 1.2

$$\sigma = \frac{N_{det}}{\Omega * N_{inc} * N_t} \tag{1.2}$$

where,

N_{det}: number of detected particles

Ω: solid angle
N_{inc}: number of beam particles
N_t: number of target particles

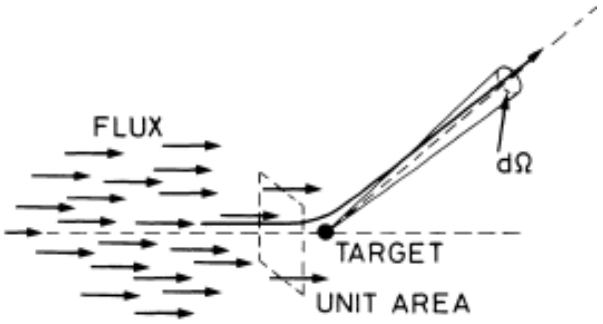

Figure 1.1: Cross section definition

The products of a nuclear reaction are not evenly distributed at all angles, therefore, in most of the cases, the differential cross-section is used [9]. Differential cross-section represents the probability of the beam particles with energy E (E_{lab}) to react with the target nuclei, emitting an ejectile at an angle θ, for the NRA scenario.

$$(\frac{d\sigma}{d\Omega})_{E,\theta} = \frac{N_{det}}{Q \cdot \Omega \cdot N_t} \tag{1.3}$$

where $\frac{d\sigma}{d\Omega}$: the scattered probability current in the solid angle dΩ divided by the total incident probability passing through a unit area of the target, and Q: the beam charge on the target. [10]

1.1.2 Stopping power

When charged particles or ions penetrate matter, they undergo energy loss, due to inelastic collisions with the electrons or collisions with the nuclei of the material. Given that the particle's probability of interacting with electrons is approximately 1000 times higher than the corresponding one with nuclei, electrons are primarily responsible for this loss and, consequently, stopping power.

During these interactions, charged particles transfer energy to the particles of the material causing ionization and excitation. The amount of energy being transferred in every collision is just a small percentage of the particle's total kinetic energy however, the number of occurring collisions is large. Summing up the effect of all collisions, the total energy loss is substantial, even for thin layers of material.

Depending on the type of the ion, its energy, and the elements on the target, the amount of energy loss varies.

1.2 Ion Beam Analysis techniques (IBA)

One of the basic advantages of Ion Beam Analysis techniques is depth profiling, the determination of the isotopic composition of a material relative to its depth beneath the surface. A group of techniques using accelerated ion beams to quantify chemical elements either on the surface or in depth of a sample by detecting particles or radiation emitted following the interaction between the beam and the target. They are widely used especially due to their non-destructive nature and high precision (error is usually below 5%). IBA can provide a depth profile of some μm, due to high energy loss. However, these techniques are constrained by the limitations coming from the use of an ion accelerator that cannot be portable. The sample target has to be delivered in the lab and be able to sustain high vacuum. Of course, some techniques support in air measurements, but they come at the expense of accuracy.

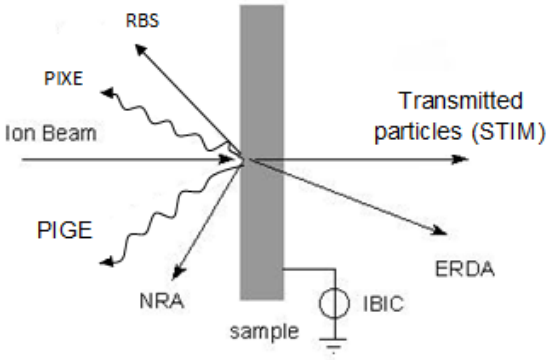

Figure 1.2: Target, beam, and detector geometry

Over the years, numerous ion beam analysis techniques have been developed, and categorized based on the products of their interactions, such as protons, alpha-particles, gamma radiation, etc. Depending on the technique used, the experimental approach, setup, and placement can be different as the emitted particles may vary, as indicated in figure 1.2 above.

1.2.1 Nuclear Reaction Analysis (NRA)

Nuclear Reaction Analysis (NRA) is considered one of the most sensitive among depth profiling ion beam analysis techniques. For some elements, concentrations can be measured down to ppm level, as for particle-gamma reactions with a sharp resonance even nanometer depth resolution can be achieved. [13] It offers two distinct methodologies [2], namely the resonant reaction method and the energy analysis method for the products resulting from charged particle reactions. Regarding the resonant reaction method, the depth profile is obtained from the incident energy

scan. On the other hand, in the energy analysis method, the energy spectrum of a reaction product is detected and the depth profile is extracted in a way similar to RBS. A relatively smooth cross-section is essential for simple data analysis using the latter method.

When the beam energy exceeds the Coulomb potential barrier of beam-target nuclei, there is an observed increase in the probability of inelastic scattering events. Those events occur because of nuclear reactions with charged particles or photons as detected products. The energy of the products relies on the reaction's Q-value.

$$E = E_{beam,m} + Q - value$$

Where Q-value stands for the amount of energy released during the nuclear reaction.

$$Q = (\Sigma m_i - \Sigma m_f) \cdot c^2$$

In exothermic reactions (Q > 0), in contrast to endothermic reactions where Q < 0, the kinetic energy of nuclei increases due to the released energy. In this case, the spectra have well-defined peaks without background interference. This method is suitable for studying light elements incorporated in heavy matrices but requires known experimental differential cross-section datasets.

1.2.2 Secondary ion mass spectrometry (SIMS)

Secondary Ion Mass Spectrometry (SIMS) is a surface analysis technique with a wide range of applications in Material Science for at least the last 40 years. This method is a combination of sputtering and mass spectrometry suitable for depth profiling and imaging of solid surfaces and thin films. [2] A three-dimensional chemical map can be created when combining depth profiling and imaging.

Sputtering is achieved by irradiating the surface of the sample with an ion beam (usual range 250eV-30keV). The primary ion generates an intense but short-lived collision cascade (figure 1.3) and many atoms of the matrix are relocated. [14] Some of the atoms near the surface receive enough energy to leave the surface; these are the sputtered ions. Thus the material under investigation will be gradually eroded.

The ejected secondary ions are electrically charged and can be carried by electric and/or magnetic fields to a mass spectrometer. There their mass/charge ratios are measured to determine the stoichiometry of the sample.[15] This method has trace element sensitivity, capable of sub-nanometer depth resolution and lateral resolution of 5nm.

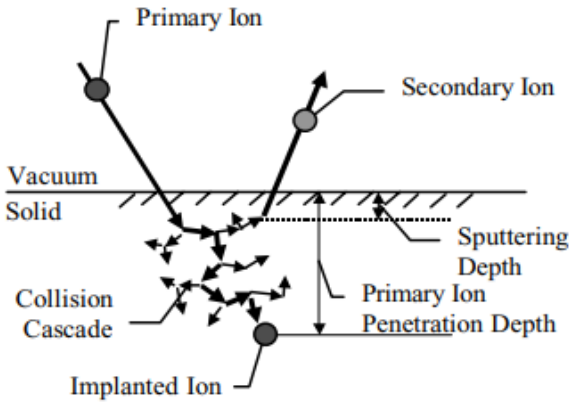

Figure 1.3: Collision cascade in SIMS. The primary ion rests after a series of collisions during which displacements of the sample atoms occur. Some secondary species are ionized and used for this technique. Typically the range of the primary particle is 1-20nm, depending on the beam energy used. [16]

Due to the large variation in ionization probabilities among elements sputtered from different materials, it is necessary to compare the results against well-calibrated standards in order to achieve accurate quantitative results. This problem is also referred to as preferential sputtering.

SIMS can be combined with ToF (Time of Flight) methods if a time-of-flight mass analyzer is used. ToF is explained further in the ToF ERDA section.

1.2.3 Time of Flight Elastic Recoil Detection Analysis(ToF ERDA)

ERDA is an IBA technique based on elastic scattering. It uses a heavy ion beam that collides with the target and causes the nuclei of the sample to recoil, which are then measured. The measurement is performed at forward angles enabling to detect species lighter than the projectiles. The number of particles detected depends on the number of incident ions and the scattering cross-section. In the case of the heavy ion beam, the scattering cross section can be calculated by Rutherford's formula because of the strong Coulomb interaction and the almost absence of nuclear force effects.

ToF (=Time of Flight) is a method using two time detectors to determine the time a particle needs to travel a specific distance. Considering that particles with different masses have different ToF, this technique helps with the identification of the particles based on their mass.

When ERDA and ToF are combined, energy and time of flight are measured simultaneously, using two time detectors for ToF and one energy detector for ERDA, placed as shown in figure 1.4. ToF ERDA measurements analyze several elements and isotopes simultaneously. [17] ERDA creates an energy spectrum and ToF provides mass discrimination of the peaks simplifying the spectrum analysis. The

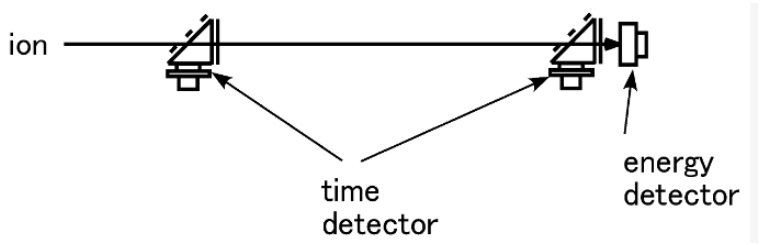

Figure 1.4: Schematic of TOF ERDA setup [18]

composition of the sample is then determined as a function of depth. Despite that, it is not always easy to discriminate different isotopes of an element as evident in figure 1.5.

The Time-of-Flight Elastic Recoil Detection Analysis (ToF-ERDA) method is one of the ion beam analysis methods that is capable of analyzing light elements in a sample with excellent depth resolution. [18]

1.2.4 resonant Particle Induced Gamma-ray Emission (r-PIGE)

PIGE is classified as a subcategory of NRA, emitting gamma radiation. The target's nuclei at rest are slightly oscillating. When bombarded by a light element beam, they gain energy resulting in either greater oscillations or nuclear reaction. In both cases, the nuclei reach an excited state and then decay to the ground state emitting gamma radiation. The gamma rays are unique for each isotope and their total yield reflects the average concentration of the target element in surface layers. This technique resembles SIMS sensitivity but is also non-destructive. It allows rapid analysis of multiple samples at a time.

The differential cross section of nuclear reactions for most of the light nuclei (Z<30) displays strong, sharp resonances when induced by light ions at low bombarding energies (<3MeV). This feature is used for depth profiling using the r-PIGE technique. A typical example of such reactions employed in light-element depth profiling is (p,γ) proton capture reactions.

The sample is bombarded with particles having energy equal to, or higher than the resonance energy. In resonance energy regions the yield of the gamma rays is much greater than the neighbor energies. Therefore, the gamma rays detected originate from the reactions taking place at the depth where the bombarding energy is equal to the resonance energy. If the energy of the beam corresponds to the energy of a narrow resonance, a resonance reaction can take place only on the surface and a surface analysis is achieved. At higher bombarding energies, the beam particles will slow down inside the sample due to energy loss. That is until they reach the depth where the decreased bombarding energy reaches the resonance energy, and the nuclear reaction occurs. By changing the energy of the beam step by step, a layering depth profiling can be achieved. [8]

1.3 ^{18}O study

The investigation of oxygen is quite important as it is highly active, penetrates materials in depth, and causes oxidization to metals changing their physicochemical properties. The importance of these characteristics is amplified by the fact that oxygen can not be easily removed from samples as it is part of the very atmosphere. The main methods applied for the study of ^{18}O, which is the isotope of interest for the present work, are presented here

Before 1960 the main method used to study ^{18}O was secondary ion mass spectrometry (SIMS). Initially, the oxygen compounds under analysis were converted to a simple gas such as oxygen, carbon monoxide, or carbon dioxide for isotopic analysis. This preparation was adopted because, except for simple molecules, the fragmentation of the original compound results in a complex mass spectrum that is not easy to study and extract information from.

In certain cases, infrared spectrometry was employed for the isotopic analysis of ^{18}O in surface layers. However, this method is limited in sensitivity and cannot be generally applied unless accurate relative absorption intensities can be determined.

In an effort to avoid these problems, mass spectrometry has gradually been replaced by activation analysis. This method requires that the product nuclide has a sufficiently long half-life in order to be detected and counted accurately. Additionally, it should be distinguishable from all the other nuclear products of the reaction. For each isotope's study, there are reactions more or less suitable, depending on the desired energy range of the measurement, the atomic number of the elements, and the reaction products under study.

The use of thermal neutron capture e.g. $^{18}O(n,\gamma)^{19}O$, for analyzing ^{18}O, could be an option theoretically. However, this method faces limitations such as the short lifetime of the product-nuclide ^{19}O (29 seconds), a low capture cross-section, and the appearance of significant background due to competing reactions. Despite these challenges, this approach has been suggested [3] for determining oxygen content in water and various compounds.

A more practical nuclear reaction for activation analysis of the ^{18}O, is the $^{18}O(p,n)^{18}F$ reaction [19], which however requires bombarding energy above 3Mev. Due to competing reactions, the counting of the reaction products has to be delayed for at least 2 hours, as they produce positron emitters with half-lives up to 20.5 minutes. Additional problems arise as many elements with middle atomic numbers have a low threshold for (p,n) reactions and high cross-section, resulting in high long-lived activities masking the final result. Besides the maximum sensitivity limit of the (p,n) reaction is of the order of 10^{-8}mg of ^{18}O. This technique has however been used (Condit and Holt) for the study of oxygen diffusion and inclusion in metals. The risk of competing reactions causing difficulties in analysis is still high.

In 1963, the $^{18}O(t,a)^{17}N$ reaction was studied [20]. The produced ^{17}N has a half-life of 4.14 seconds and decays by beta emission to an excited state of ^{17}O,

which then emits a neutron and returns to ^{18}O. While this delayed neutron emission is highly specific to ^{18}O, this method requires an accelerator capable of providing tritions.

The same year (1963) G. Amsel proposed an alternative method that suggested direct detection of the charged particles emitted because of the nuclear reaction. One year later [5] he published his experimental trials of this method studying the reactions $^{16}O + d$ and $^{18}O + p$, setting the base for the newly found nuclear reaction analysis (NRA) method. The second reaction is also the one investigated in this thesis. Expanding his research with various reactions [21] it became obvious that the reactions producing alpha particles or protons are the simplest ones. Those are easily detected by semiconductor detectors that are virtually background-free.

Of course, ^{18}O was approached from the resonance point of view, as it presents various narrow resonances valuable for depth profiling purposes. The most important is probably the one at 152keV in $^{18}O(p,\alpha)^{15}N$ reaction studied by G. Battisting in 1991 [22]. The significance lies in the fact that, with $\Gamma = 50eV$, it is considered a very narrow resonance and therefore valuable for various measurements e.g. thickness measurements.

Techniques like RBS and EBS are excluded from the ^{18}O study due to their tendency to cause oxidation with heavy elements, which is highly prohibitive for elastic scattering measurements. Meanwhile, the detection of gamma rays with PIGE is not suggested as it displays lower cross-section values. PIXE on the other hand does not allow isotope discrimination.

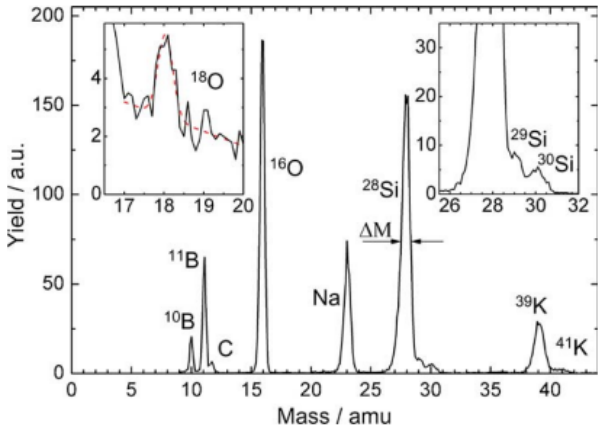

Figure 1.5: Mass spectrum from events during TOF ERDA experiment. Inserts demonstrate the separation of oxygen and silicon isotopes. [24]

Oxygen, and specifically its isotope ^{18}O, is also approached with TOF-ERDA ([24], [25] and [26]), and generally the quality of the results is considered comparable with those obtained by NRA [27]. However, the method itself, apart from being superficial, is related to problems in statistics and the discrimination of the isotopes on the spectrum. In figure 1.5 although the peak from the ^{18}O isotope is

sitting on the smooth tail of the much stronger ^{16}O signal (^{18})/$^{16}O = 2 \cdot 10^{-3}$), the two oxygen isotopes are clearly separated.

NRA is undoubtedly one the most efficient methods for studying ^{18}O and as such, it is employed for the current measurement. Still, other techniques are also tested, most of them combined with ToF to overcome the difficulties accompanying a complex mass spectrum. Mass spectrometry was employed again as TOF-SIMS and GD ToFMS (=Glow Discharge Time Of Flight Mass spectrometry) [23] providing satisfactory results.

1.4 ^{18}O(p, α_0)^{15}N Reaction

Proton beams are most commonly used for this type of measurement due to their suitability for isotopic quantification. The (p,α) reaction, in particular, was chosen for its high Q-value, which separates the studied peak from the elastic peaks, facilitating the analysis. Compared to the $^{18}O(d,\alpha)$ reaction, it offers a higher cross-section, making the experiment more straightforward. Additionally, using a deuteron beam carries the risk of neutron emission if an energy threshold is exceeded.

The Q-value for the production of the compound nucleus ^{19}F is 7.993 MeV, whereas for the final product, ^{15}N, it is 3.979 MeV.

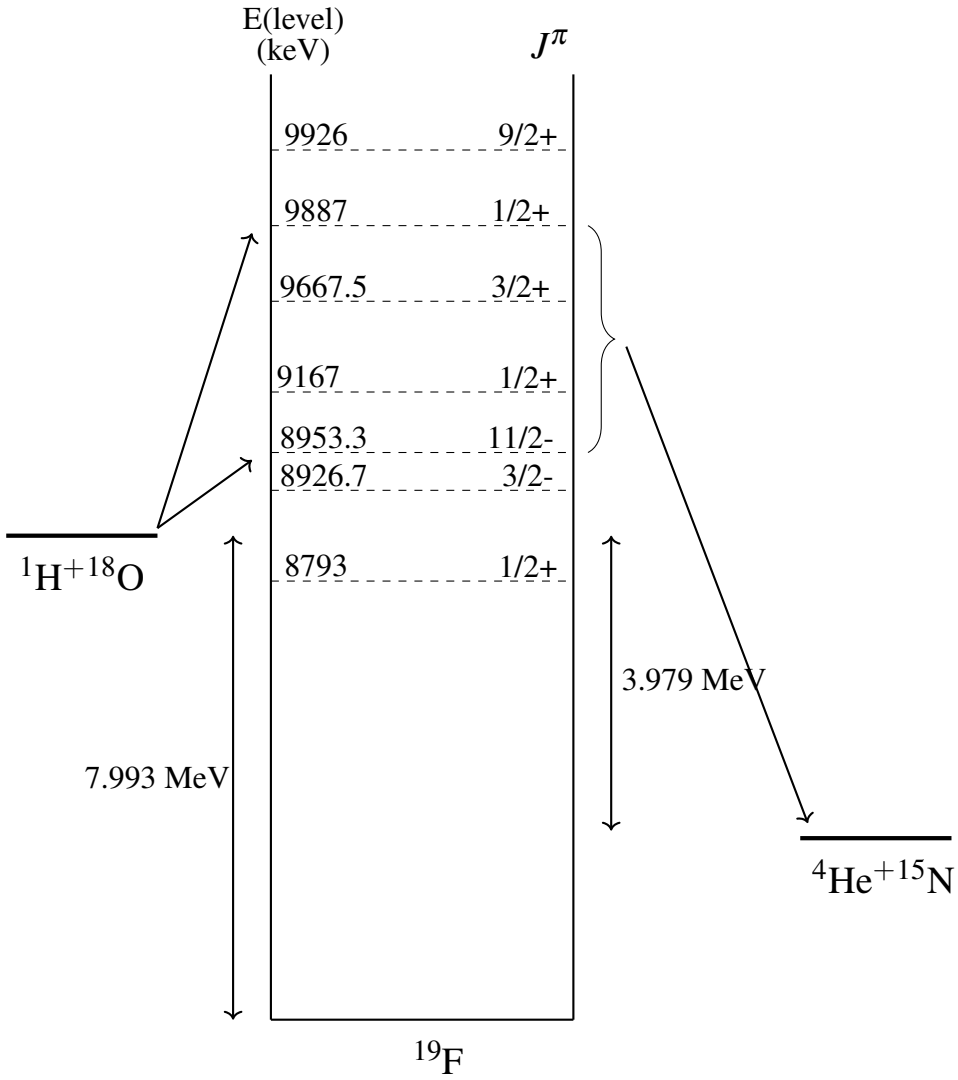

Figure 1.6: Energy scheme of compound nucleus ^{19}F

Chapter 2

Experimental Equipment

2.1 Accelerator

The experiment took place at the Institute of Nuclear and Particle Physics of NCSR "DEMOKRITOS" in Athens, Greece, employing a Tandem Van de Graaf accelerator. It is a linear electrostatic accelerator (T11 5.5 MeV), based on a Van de Graaf generator to which it owes its name.

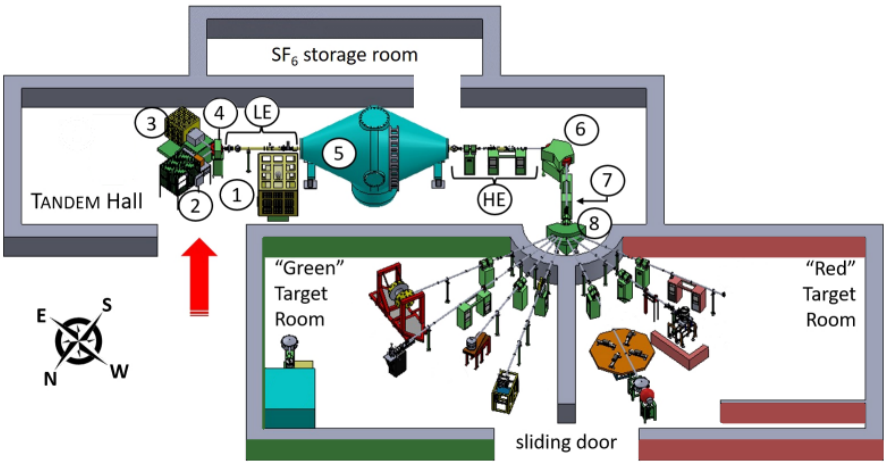

Figure 2.1: Schematic representation of the accelerator facilities [28]

The main parts of the accelerator are presented below following the numbers in figure 2.1. The symbols "LE" and "HE" indicate Low Energy and High Energy beam-line respectively.

From 2021-2022 the accelerator underwent a major upgrade through the CALIBRA project, aiming at expanding its beam production capabilities. While the main function logic remained the same, the basic parts were replaced allowing for higher vacuum and higher current intensity, thus optimizing the operation of the accelerator.

Table 2.1: Basic structural elements of the accelerator

Number	Description
1	Electronics Faraday Cage
2	Torvis ion source
3	Snicks ion source
4	30^o inflector magnet
5	Tank hosting the Generator (terminal)
6	90^o analyzing magnet
7	Poststripper
8	Switching magnet

The diffusion (oil-based) pumping stations were replaced with new turbo-molecular ones, allowing the vacuum in the accelerator tube to be kept under 10^{-7}mbar. Collisions between beam ions and air particles cause attenuation of the beam. The energy of the beam should not be decreased and therefore the air particles are extracted by achieving a high vacuum. The higher the vacuum, the less the energy loss. In this direction, the accelerator beamlines are equipped with full-range vacuum gauges.

In the framework of ion source upgrading, the old ion sources were removed along with their associated power supplies and the pre-acceleration tube. The Duo-plasmatron and Sputter ion sources were replaced with a TORVIS and a SNICS sputter source respectively. They were both accompanied by their fiber-optics controlled power supplies enclosed in their safety cage. Each source operates at a 55 kV pre-acceleration potential. Moreover, the TORVIS source is equipped with an ion exchange Rubidium exchange canal. Extensive testing on the performance of the TORVIS ion source produced a beam of 100 μA with low angular divergence for both H^- and D^- beams. During this experiment, a proton beam was used and the TORVIS source was employed, which is suitable for lighter ions. Unfortunately, the intensity of the current could not exceed 100nA due to the thickness of the target, causing pile-up effects. The SNICS source produces heavier ions such as Carbon, Oxygen, etc. Ions with charge e^- are produced from the sources at the beginning of the line.

The direction of the beam traveling through the tubes is adjusted by a series of magnets along the tubes. The inflector magnets change the direction of the beam. For example, the analyzer magnet (energy selection magnet) turns the beam by 90^o and allows ions only with specific energy to continue their course. The switcher magnet directs the beam toward one of the experimental lines and another inflector magnet allows the ions to enter from the right source. There are also quadrupole magnets along the beam line focusing the beam.

The main part of the accelerator is, of course, the tank containing the Van de Graaf generator in SF_6 gas under pressure of about 6 bar where the ions gain

their main acceleration. SF_6 is an insulating and suppressing gas and increases the maximum voltage where electrical discharges start in the tank, which is harmful to the accelerator system. This is what limits the maximum operating voltage to 5.5 MeV.

During the upgrade, the accelerator charging system and the stripper canal along with their associated electronics were replaced. The old electrostatic belt was replaced with three Pelletron© chains to maintain the maximum charging capability of the terminal. Also, two new stripping systems were installed in the terminal based on different functions. One offers foil stripping, being able to host 80 carbon foils, and the other is a gas stripper operated with nitrogen. Currently, only the gas stripper (figure 2.2) is in use. The stabilization of the terminal voltage is achieved with the aid of four separate systems namely a Capacity Pick-Off plate, a Generating Voltmeter, a Corona probe, and the analyzing slits.

Figure 2.2: The new stripping canal in the accelerator tank [29]

The terminal is positively charged by the Pelletron chains at the higher voltage. Therefore when the negative ions from the source enter the tank, they are attracted by the terminal. There the stripper strips the ions of their electrons, converting them to positive ions, now repelled by the terminal towards the exit of the tank.

In total the ions in the accelerator tank gain energy

$$E = q_{before}V + q_{after}V, \tag{2.1}$$

όπου $q_{before} = e^-$ and V the terminal voltage.

The walls of the Tandem Hall and the two Target Rooms are shielded with concrete enriched with Barium, because of the emitting radiation (alpha, beta, gamma, and neutrons) which should be restricted for safety reasons.

2.2 Detectors

For this experiment, six Silicon Surface Barrier (SSB) detectors were employed for the detection of alpha particles at different angles. Furthermore, a high-purity Germanium detector (HPGe) was used to serve for the accelerator calibration.

Both of them are semiconductor diode detectors and therefore based on semiconducting, crystalline materials. Silicon (Si) and Germanium (Ge) are two of the most commonly used materials, with the first mainly used for charged particle spectroscopy and the latter employed for gamma-ray measurements. Semiconductor detectors are, in general, compact and offer very fast response time. Additionally, in comparison with any other common detector type, they can result in a much higher energy resolution for a given incident radiation.

Excluding the silicon ones, the rest of the semiconductor detectors require cooling at low temperatures before use. A signal is detected when an electron jumps from the valence to the conduction band surpassing the energy gap. If a similar effect occurs spontaneously and not as a result of ionizing radiation, the experimental measurements will be clouded with background noise. If the semiconductor is cooled, the kinetic energy of the electrons is reduced causing almost all of them to fall into the valence band decreasing the conductivity of the semiconductor and therefore the noise incidents.

2.2.1 Silicon Surface Barrier (SSB) detector

For the detection of charged particles, the most widely used detectors are the silicon ones, specifically Silicon Surface Barrier (SSB) detectors. This type is employed for this experiment for the detection of alpha particles. It consists of an n-type silicon crystal and a thin layer of gold deposited on silicon by evaporation for electrical contact. The back of the crystal is covered with aluminium which acts as resistive contact transforming the detector into a capacitor with silicon as the dielectric material.

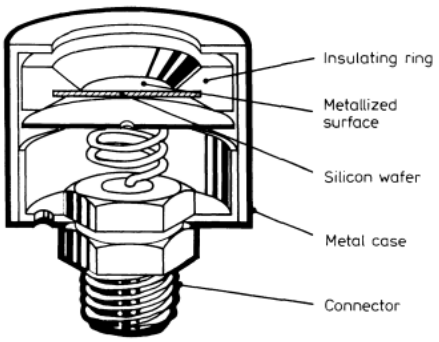

Figure 2.3: Cross-sectional schematic of a surface barrier detector [11]

SSB detectors exhibit sensitivity to light. Given that they detect photons and the energy of visible light photons (2-4 eV) is greater than the forbidden energy gap of most semiconductors, any external light source is enough to contaminate the measurements. [10] Most experiments require a vacuum enclosure and the detector can be placed inside the chamber thanks to its small size, also shielding it from the room light. Considering that SSB is an open detector it should be handled

carefully as it is sensitive to surface contamination. Even contact with the skin would leave oil traces on the surface, absorbing part of the energy before it reaches the crystal.

The operating voltage range is 50-300V, with the ones employed for this experiment to operate on 50V.

2.2.2 High Purity Germanium detector (HPGe)

Germanium detectors offer the highest resolution available for gamma-ray detection and thus are preferred for this machine calibration, as the reaction employed was $^{27}Al(p,\gamma)^{28}Si$. The photoelectric cross section is 60 times greater in Ge than in Si, granting the Ge detectors with great efficiency levels.

The higher the applied voltage is, the more the depletion region expands until it covers the whole crystal. HPGe detectors are generally operated as fully depleted detectors. However, because of the small band gap of germanium (0.7eV), the detector should always be operated at low temperatures to avoid, or at least reduce, the thermally induced leakage current which causes noise and reduces the energy resolution. The cooling of the crystal is achieved with liquid nitrogen bringing the temperature down to 77K. The detector is accompanied by an insulated dewar, keeping the liquid nitrogen in thermal contact with the detector. Unfortunately, the size and weight of the dewar, which are much greater than the detector's, restrict its portability. The germanium crystal must be housed in a vacuum-tight cryostat to prevent thermal transfer from the surrounding air.

Germanium detectors hold an interesting feature and proved to be a strong manufacturing advantage. They offer the "test" function, which allows the detector to collect artificial signals (e.g. from pulse generators) carrying known and stable data. This feature is ideal for controlled tests before the actual experiment.

2.3 Electronics

2.3.1 Preamplifier

It is easy for the preamplifier to be interpreted as the first stage of amplification of the pulse, although this is not its main purpose. Specifically, a preamplifier is bound to collect the signal and drive it toward the amplifier. [10] It provides a high-impedance load for the detector and a low-impedance source for the amplifier, shaping the subsequent output pulses.

Given that the signal at the preamplifier is generally weak, it is essential to keep the noise at the lowest possible levels. Usually, a preamplifier is mounted directly on the detector minimizing the in-between cable length and consequently the cable capacitance which decreases the signal-to-noise ratio.[12] The rise time of a preamplifier must be smaller compared to the detector's so that the effective rise time is determined by the detector and not by the preamplifier.

2.3.2 Amplifier

Amplifiers serve two main purposes by amplifying the signal from the preamplifier and shaping it to a convenient form for further processing from the rest of the equipment. Depending on the information of interest, which must always be preserved, there are fast amplifiers providing timing information and spectroscopy amplifiers determining the pulse height. The second type is the one required for this experiment.

The pulse produced by the preamplifier is an exponential sharply peaked pulse with a long tail, which does not allow the direct measurement of the pulse height. Therefore, pulse-shaping offered by the amplifier is an important function. The input signal is first differentiated and then integrated producing almost Gaussian-shaped pulses proportional in amplitude to the input pulse. By shortening the tail, the pile-up effect is decreased and the signal-to-noise ratio is optimized.

Most amplifiers provide additional features to assist their performance at high count rates, such as pole-zero cancellation, shaping time, baseline restoration, and pile-up rejection.

2.3.3 Analog to Digital Converter (ADC)

An ADC is the link between analog and digital electronics. The information remains unchanged but is converted from an analog to a digital form. Its resolution depends on the range of the digitization, meaning the number of digits acquired. The digitization process lasts for what is called conversion time. For most ADCs it extends for a duration typically in the range of several tens of μs or more, categorizing them as slow devices compared to other NIM modules. [10]

2.3.4 Dead time

Dead time represents the finite minimum duration required between two events, to be recorded as distinct pulses [10]. It is the fraction of real time during which the system can detect and measure events, divided by the live time of the measurement. Typically, this parameter is associated with the pulse duration and the ability of the detector to distinguish between individual pulses before they overlap. In the specific experimental setup, the Analog-to-Digital Converter (ADC) is identified as the component with the slowest response time, becoming the primary cause of dead time.

To increase the accuracy of a measurement, the dead time should be accurately known and limited preferably below 10%. Especially for a dead time greater than 30-40% of the total real time of the measurement, the counting rate is too high, leading to pulse pile-up and unreliable measurements. To minimize dead-time effects, the possibility of a second event occurring during the dead-time period should be weak. Thus the counting rate of the detector must be kept sufficiently low. Of course, the probability of an event loss is never eliminated due to the random nature of radiation emission [11].

2.3.5 Pile-up effect

Pile-up is the aftermath effect of high rates of dead time. The output of a preamplifier is a tail pulse with a long decay time, from $\tau \simeq$ few $\mu s - 100\mu s$. If a second signal arrives within this period, it will ride on the tail of the first, as shown in figure 2.5 and will not be recognized as separate events. The resulting output pulse will be equivalent to the height of the first pulse received increased by a proportion of the height of the second pulse. [12] This proportion depends upon how close they arrive.

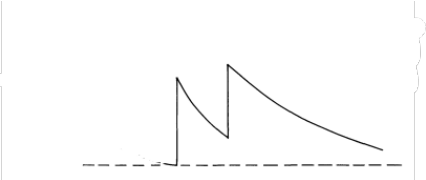

Figure 2.4: Pulse pileup. A second pulse rides on the tail of the first [10]

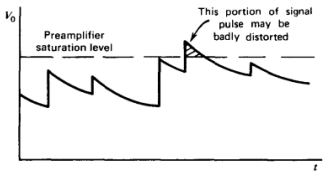

Figure 2.5: Pulse pile-up in the preamplifier at high rates. [11]

To avoid this troubling effect the counting rate must be less than $1/\tau$ counts/s which is not always achievable as it is mainly related to the target. For example, thicker targets offer higher counting rates respectively. As an alternative, the tail of the pulse must be shortened. This is usually achieved by preamplifiers and amplifiers reshaping the pulse. For this experiment, the shaping time was set at the lowest possible value to reduce the pile-up effect. However, in this scenario, although the detectors can detect the signals promptly, the ADC's high dead time prevents it from registering them, resulting in pile-up. In figure 2.5 the piled-up outcome of a preamplifier is depicted. The saturation level marks the limit above which the pulses may be distorted. In specific cases, protective films like Mylar (section 5.1) are employed to reduce the counting rate.

2.4 Chopper

While usually the electrical charge of a beam in a spectroscopy experiment is measured using the Faraday cup, some situations require a different approach. In this case, the thickness of the target does not allow the beam to pass through and reach the Faraday cup. A frequent alternative is the use of a chopper acting as a reference point. As depicted in figure 2.6, a chopper consists of one or more blades, a motor enabling them to rotate, and an SSB detector. The blade allows and cuts the beam periodically at a predetermined frequency. This approach allows the beam to be monitored without disrupting the main measurements.

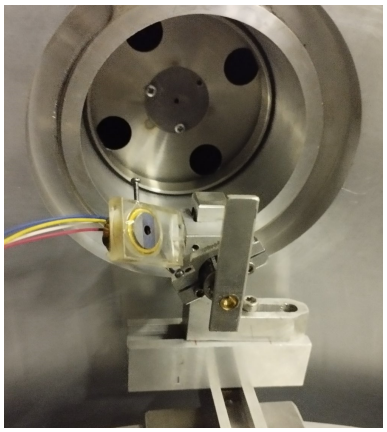

Figure 2.6: Photo of the chopper mounted in the entrance of the chamber

A chopper is basically a separate experimental setup with a well-known target and its own detector monitoring the reaction. Knowing the cross-section, yield, and thickness of the target, the charge of the beam can be easily calculated. As both this and the main reaction are triggered by the same beam, they share the same properties regarding the beam and thus the same electrical charge.

The chopper used for this experiment has one blade consisting of a thin layer of ^{197}Au on thick Aluminium. It is programmed via Arduino to interrupt the beam for 1 second every 9 seconds, monitoring its properties.

2.5 Experimental setup

2.5.1 Instumentation

The instrumentation was arranged in the Red Room located in the Tandem Laboratory at N.C.S.R. "Demokritos". A high-precision goniometric chamber, shown in figure 2.7, was employed. During the experiment, the chamber was sealed and high vacuum conditions were sustained in the order of 10^{-6} mbar by a turbopump. The target was mounted on a holder in the middle of the chamber, perpendicular to the beam. The particular holder can host multiple targets and allows both vertical and rotational adjustments from outside the chamber.

Six SSB detectors were secured on rails in the chamber covering the backscattering angles 170^o, 160^o, 150^o, 140^o, 130^o, and 120^o.However, the detector positioned at 120° was disconnected before the experiment began, so it will not be mentioned further. The exact distances for each detector from the target are given in table 2.2. Detectors were equipped on the front with slits and tubes to minimize the random scattering distributed throughout the surrounding space. Slits are tantalum masks with rectangular openings with widths, in this case, from 3 to 5 mm, attached directly in front of the detectors. The length of the tubes varied from 3.7 to 6.5cm. The theoretical minimum distance of the detectors provided in table 2.2,

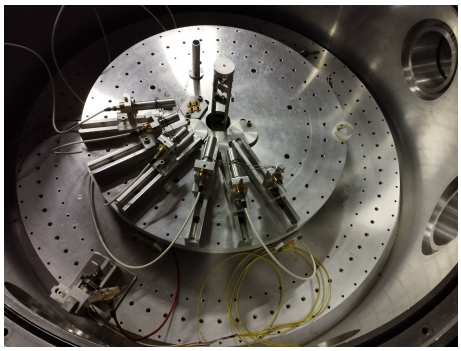

Figure 2.7: Photo of the interior of the goniometric chamber with mounted detectors

are calculated approximately by the formula $(slit\ \ diameter : 2) : tan(1^o)$. The detectors were mounted at slightly different distances to maintain a clear line of sight for all of them.

All tubes are grounded in the chamber to avoid charge build-up.

Table 2.2: Measurements from Detector Placement

ϑ (deg)	**170**	**160**	**150**	**140**	**130**
canon length (cm)	3.7	5.2	3.7	5.4	6.5
slit diameter (mm)	3	4	5	5	5
distance from target (cm)	9.5	11.5	14	13.7	14
theoretical ideal distance (cm)	8.6	11.5	14.3	14.3	14.3

Unfortunately, data acquisition was restricted to the detectors monitoring angles of 170^o, and 160^o. The detector positioned at 150^o experienced electronic malfunctions, and the data from the remaining detectors were non-analyzable due to insufficient statistics of events.

Two collimators, with diameters of 4 and 3 mm respectively, are positioned along the experimental line, optimizing the beam spot to $2 \times 2mm^2$. To ensure the integrity of the measurement process, the experimental chamber must be tightly sealed against any external light infiltration. The detectors are sensitive to photon detection and external light interference could compromise the accuracy of the measurements. As a precautionary measure, the lighting within the room was turned off.

Target

The implemented target consisted of a thin layer of Ta_2O_5, highly enriched in ^{18}O, created on the surface of a thick tantalum foil via controlled, progressive anodization. The target is presented in figure 2.8.

For the purposes of this experiment, a target with thin or no backing would be ideal, to avoid pile-up effects. (Thick targets are mainly suitable for cases when gamma particles are measured.) However, due to the laboratory's renovations and updates, the manufacturing of such a target was not possible.

Figure 2.8: Photo of the target on the holder before the experiment.

2.5.2 Electronics setup

The present experiment uses a straightforward arrangement of electronic modules. Initially, the detected signal is channeled through a preamplifier and subsequently routed through an amplifier, to be shaped and amplified. In this case, a shared unit for amplification and preamplification was used. Following this stage, the analog signal is converted into its digital form, using an Analog-to-Digital Converter (ADC). Finally, a Multi-Channel-Analyzer (MCA) is used to segregate the pulses into 1024 distinct channels based on their energy levels, as shown on the histogram (PC), facilitated by suitable Data Acquisition (DAQ) software.

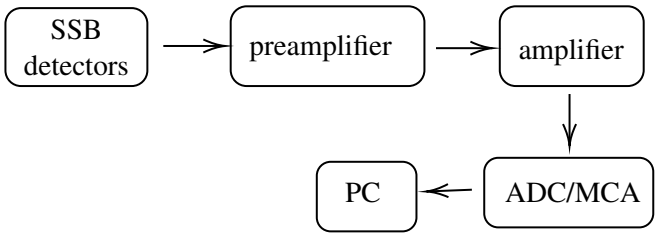

Figure 2.9: Electronics schematic

On the first day of the experiment, an attempt was made to replace the analog electronics with digitizers. However, this approach was abandoned due to a series of encountered challenges.

Chapter 3

Data analysis

3.1 Methodology

As discussed in section 1.1.1 the differential cross section is calculated using equation 1.2. Two distinct methodologies are commonly employed: relative and absolute measurement. The former involves comparing the measurement with a reference dataset obtained for another isotope. In contrast, the latter, adopted in this study, entails a direct calculation of the differential cross-section. The differential cross-section calculation was realized by experimentally determining each constituent factor of equation 1.2, and will be elaborated in the following sections.

The Ta_2O_5 target is irradiated with a proton beam, within the energy range of 1-2MeV, triggering the $^{18}O(p,\alpha)^{15}N$ reaction. The measurements were carried out with a variable energy step of either 10 or 20 keV, to map the multiple and thin resonances of this reaction. Alpha particles are produced, mainly towards backscattering angles.

For this approach, a thin target is required, to minimize beam energy loss, as the measurements correspond to the middle of the target.

3.1.1 Experimental yield

The experimental yield corresponds to the number of particles detected (N_{det}) for a specific angle. This quantity is determined by integrating the (p,a_0) peak of each spectrum across all angles for every energy level, using the SpectrW code [30]. A typical spectrum in the SpectrW environment is displayed below (figure 3.1). The selected spectrum refers to the 170^o angle for beam energy 2000keV.

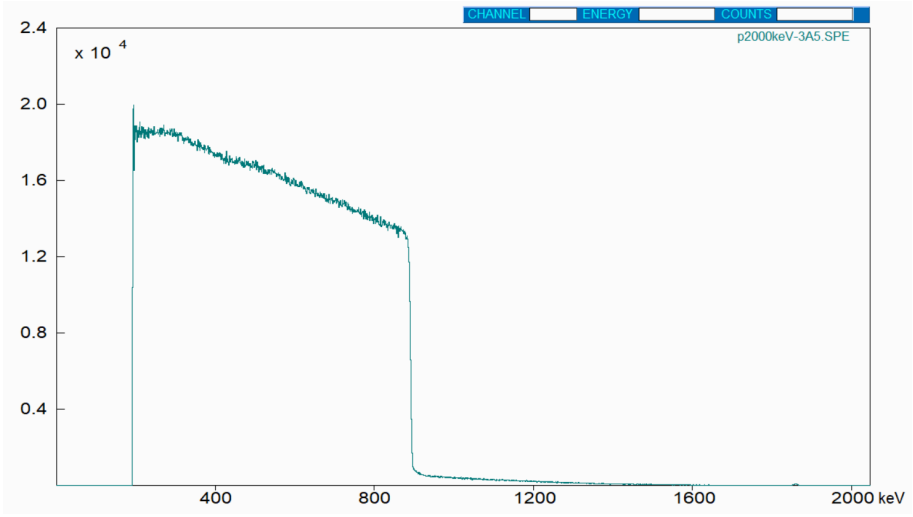

(a)

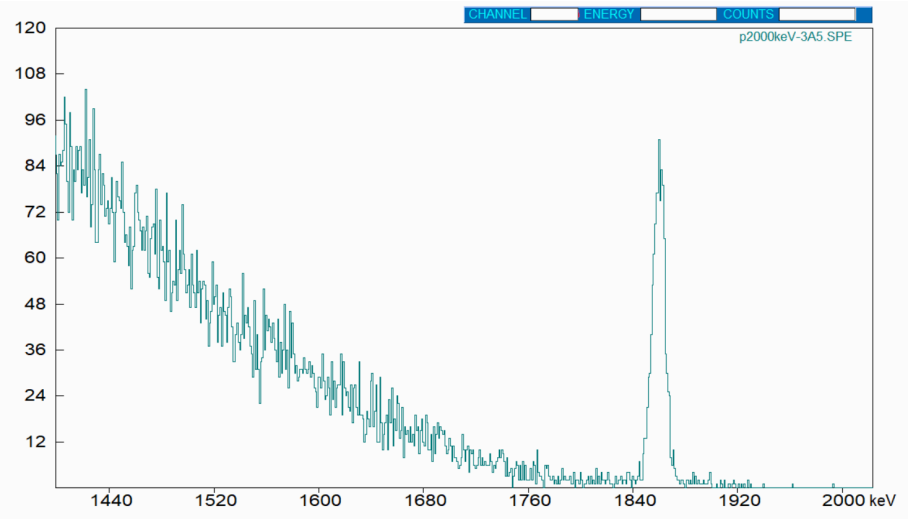

(b)

Figure 3.1: Typical spectrum of the $^{18}O(p,\alpha)^{15}N$ reaction at 170^o and 2000 keV in SpectrW environment. In (a) it is shown in full scale, where only the heavy Ta backing is visible. By zooming in the tail in (b), the analysis of the a-peak is possible.

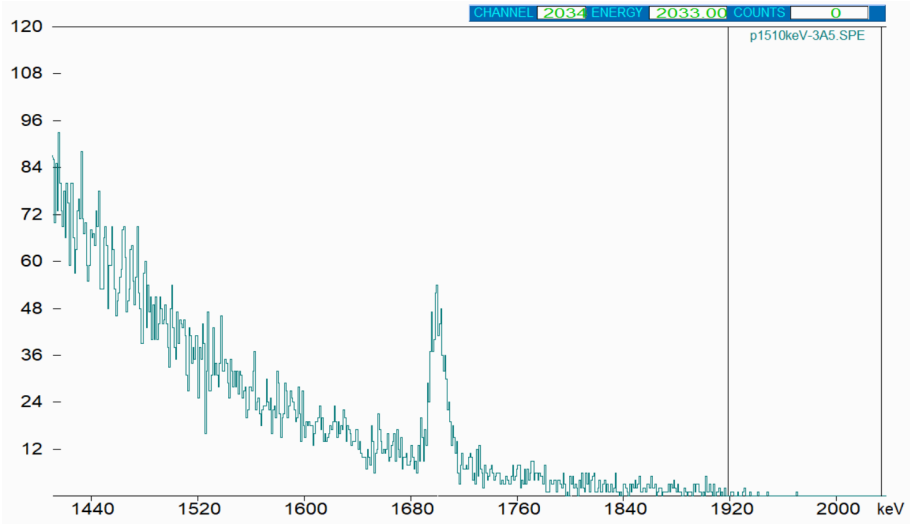

Figure 3.2: Spectrum obtained at 1510 keV. The pile-up effect is stronger for lower beam energies.

As proton beam energy decreases, the pile-up effect intensifies, as evident in 3.2 due to increasing Rutherford backscatterings from the Tantalum.

The entire peak analysis procedure is performed manually. Initially, the background is subtracted from each spectrum, by choosing 10-15 reference background points. The limits of the (p, a_0) peak are then marked, and the area is calculated through integration. Supplementary, a Gaussian fit was applied to confirm the results. Following a preliminary calculation, it was evident that the data derived from the peak integration were more reliable, as expected.

The integrated counts are accompanied by their respective errors, estimated to be approximately 3%.

3.1.2 $Q \cdot \Omega$ factor - SIMNRA simulations

The factor $Q \cdot \Omega$ presents the greatest error in the equation used to calculate the differential cross-section, where Q stands for the charge of the beam and Ω for the solid angle. In this experiment, the target is embedded on a thick backing, making it difficult to measure this factor experimentally. Measuring the charge behind the target is unfeasible due to the beam's inability to penetrate the thick target.

Direct experimental determination of the $Q \cdot \Omega$ factor is impractical. However, an attempt was made to use a chopper at the entrance of the chamber, to calculate the charge of the beam before the reaction. Unfortunately, this approach proved to be ineffective, as the significant peak blended with the background created by the chopper's backing. The data obtained were analyzed and, although not reliable enough for the final results, they confirm our anticipated outcomes. Experimental data are provided in the appendix.

Finally, this factor was estimated using SIMNRA simulations on the thick Tantalum backing.[31]. SIMNRA is a program used for the simulation of charged particle energy spectra and gamma-ray yields for ion beam analysis with MeV ions. Initially, the target is created within the SIMNRA environment by specifying the amounts of different elements, their thicknesses, and the percentage composition of each component in the target.

Several parameters are set in the simulation: the type of incident particle and its energy, the real and live time of the measurement, and the exit angle. Additionally, the energy per channel and the offset, as provided by the energy calibration diagram in section 3.2, are inputted. The resolution for the SSB detectors is set to 32.5 keV. Regarding the setup calculation, data for the electronic stopping power are used according to the ZZ+KKK model. The shape of the straggling distributions is considered an asymmetric Gaussian. For energy loss straggling, the Chu+Yang model is employed, while the Amsel model is used for multiple scattering. The screening to Rutherford cross section follows the Anderson model. Due to the presence of a thick tantalum backing, pile-up effects are significant, and hence, the pile-up calculator is activated.

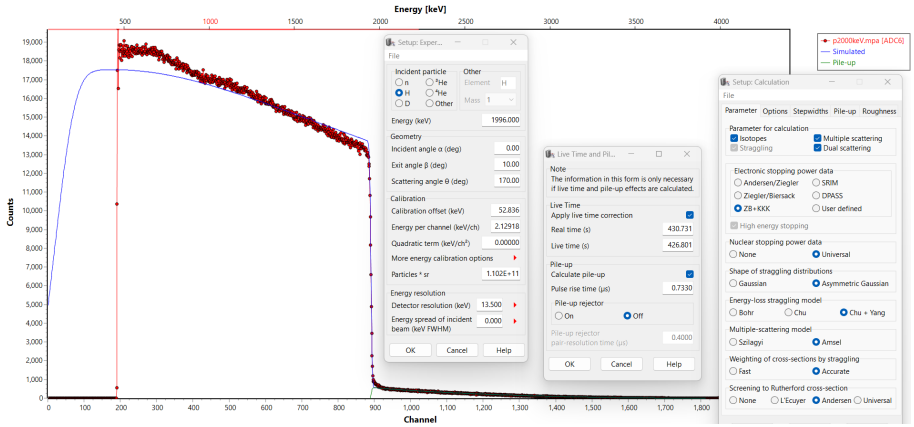

Figure 3.3: A snapshot in the SIMNRA environment. Red dots represent the experimental data and the blue line the simulation curve.

Multiple simulations are performed, each time adjusting the $particles \cdot sr$ factor and slightly modifying the pulse rise time factor, until the simulated curve closely matches the experimental one. A snapshot during the analysis is illustrated in 3.3. To verify compatibility, the experimental and simulated curves are integrated and compared in two areas: the pile-up region and an even area of the tantalum backing peak. By comparing the experimental data with the simulation, the discrepancies were consistently found to be below 1%, which is considered the error of the factor.

Based on the comparison described above between experimental data and simulation, it became evident that the pile-up simulator provides satisfying and reliable results throughout the whole energy range. The charge of the proton beam (Q) re-

mains the same for every angle as it depends solely on the beam, and the solid angle remains consistent due to the use of identical detectors. Consequently, the ratio $\frac{(Q\cdot\Omega)_{170}}{(Q\cdot\Omega)_{160}}$ should remain stable and is used to further validate the results, which it does.

3.1.3 Target Thickness

The manufacturer specifies the target thickness as $d = 326 \cdot 10^{15}\ {}^{18}O\ at./cm^2$.In the absence of a provided error, a systematic error of 10% is assumed. To validate this experimentally, we used the (d, α_0) and (d, α_1) reactions at 1900 keV and 165^o [1] for convenient statistics. The differential cross section for these reactions is known from Amsel (Amsel 1964). Namely, $(\frac{d\sigma}{d\Omega})_{\alpha_0} = 2.19 \cdot 10^{-27}\ cm^2$ and $(\frac{d\sigma}{d\Omega})_{\alpha_1} = 2.26 \cdot 10^{-27}\ cm^2$. SIMNRA was employed to simulate $Q \cdot \Omega$ for both reactions, as described above. To improve the accuracy of the simulation, simultaneous fits are performed for the two peaks (α_0 *and* α_1), and the thickness of the target. Additionally, the background was removed temporarily, to approximate better the simulation's shape (figure 3.4).

Given that this measurement was conducted separately from the main experiment, which used deuterons as projectiles, the machine calibration by [32] was employed. According to this calibration, the energy offset is 0.13 keV.

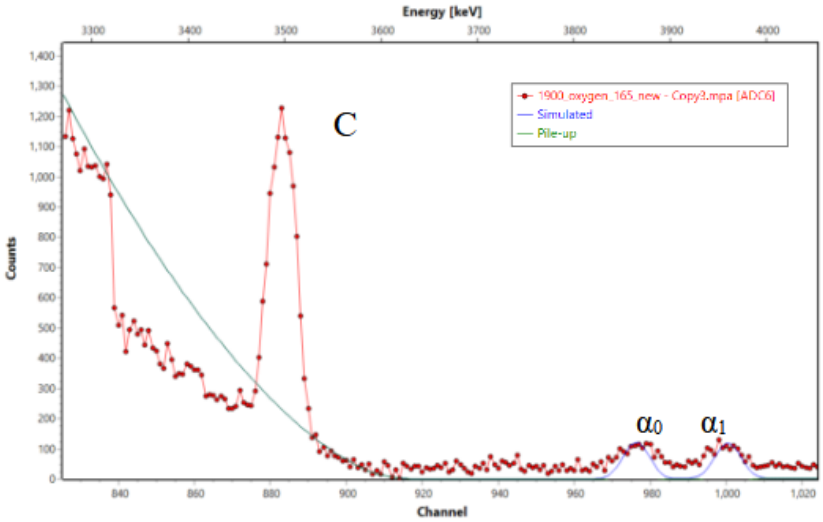

Figure 3.4: Temporary and localized background removal in SIMNRA for a more accurate simulation. The α_0 *and* α_1, as well as a carbon peak, are visible.

The yield was calculated by integrating the peaks both separately and together, using the double peak fitting feature provided by SpectrW. Separate integrations

[1] The detector is placed at 165^o, but the same energy calibration as 170^o is employed since the detector and the rest of the settings are the same.

were used for the calculations, as this method demonstrated higher accuracy. The thickness was calculated for each peak individually, and the mean value was used with the corresponding error. Specifically, the error for the thickness was not calculated by error propagation because the mean absolute error is significantly larger. The difference between the results derived from the α_0 and α_1 peaks is attributed to statistical error, as the cross-section values provided by Amsel [5] are correlated.

Table 3.1: Target thickness calculations

	dσ/dΩ (mb)	N_{det}	$Q \cdot \Omega$	N_{tar}(at./cm^2)	dN_{tar}
(d,a_0) reac.	2.19	752	$1.619 \cdot 10^{12}$	$2.12093 \cdot 10^{17}$	
(d,a_1) reac.	2.26	839	$1.619 \cdot 10^{12}$	$2.29301 \cdot 10^{17}$	
mean value				$2.207 \cdot 10^{17}$	$0.086 \cdot 10^{17}$

The calculated thickness of the target was found to be **d=**$(\mathbf{2.207 \pm 0.086}) \cdot \mathbf{10^{17}}$**at.**$/\mathbf{cm^2}$.

The experimental value of the thickness does not coincide with the one given by the manufacturer by approximately 30%. Experimentally, the target appears much thinner, requiring further study. Consequently, the cross-section values are calculated based on both the experimentally determined thickness and the thickness provided by the manufacturer. There are alternative methods for estimating the thickness. One involves using the resonance of ^{18}O at 152 keV with a width Γ=50 eV, which is thin enough to allow great accuracy.[2] Additionally, heavy ion techniques such as ToF-ERDA can be used to distinguish and quantify isotopes.

3.2 Energy calibration

Energy calibration is essential for each detector, not primarily for peak identification, but because it provides crucial information for SIMNRA simulations, specifically "energy per channel" and "offset". Given the target thickness, it is important to perform the calculation using information from the middle of the target. Therefore, both the energy for Tantalum (Ta) obtained from SIMNRA and the corresponding channel determined using Spectrw, refer to the midpoint of the Ta peak edge. This procedure is repeated every 40-50 keV.

Energy is plotted against channels and a linear fit is applied using the $y = a \cdot x + b$ function, where α represents "energy/channel" and b is the offset. These values are provided in the captions of figures 3.5 and 3.6.

[2]Due to the circumstances, a measurement could not be conducted at the initial time. The measurement was later performed in the final days of June in Bochum, Germany, by A. Lagoyannis and E. Taimpiri, with the results currently in a preliminary state.

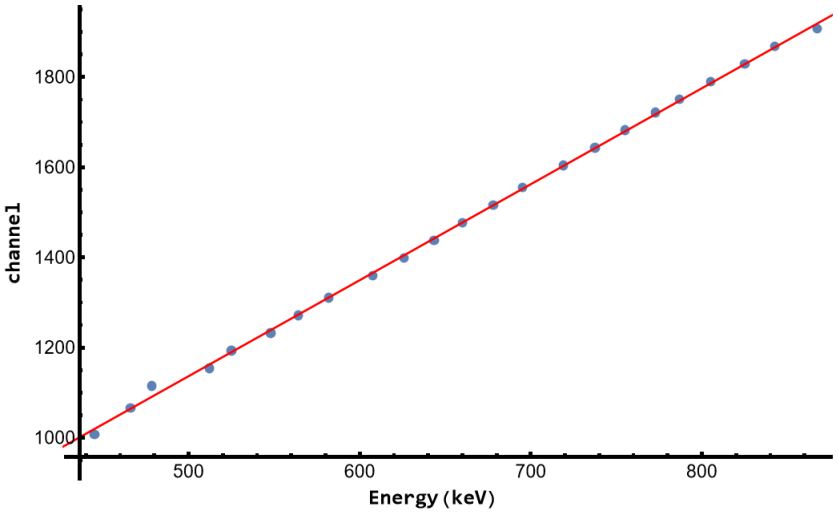

Figure 3.5: Detector energy calibration at 170^o, $y = 2.129 \cdot x + 71.836$

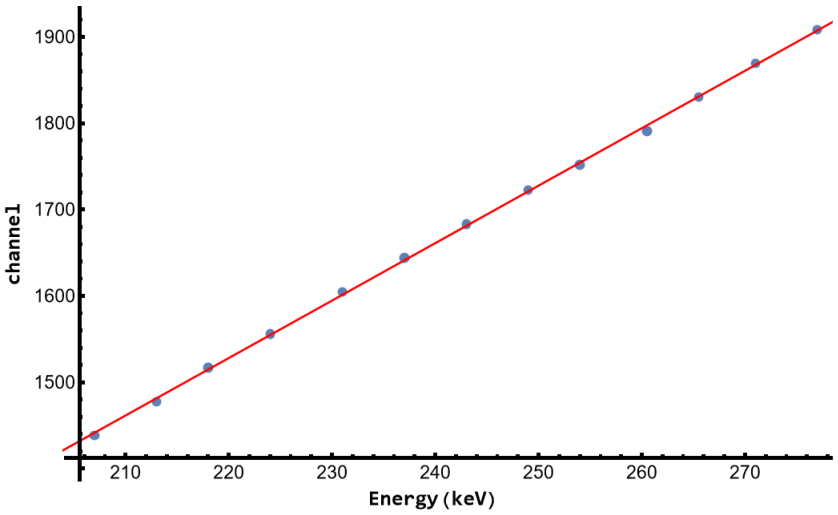

Figure 3.6: Detector energy calibration at 160^o, $y = 6.655 \cdot x + 63.84$

3.3 Machine calibration

The energy of the proton beam provided by the accelerator is described by a Gaussian distribution around the peak energy defined by the operator. Adjustments to the energy are made using magnetic fields, which can result in slight deviations from the requested energy, called offset. Consequently, machine calibration for the accelerator is necessary to reference the correct energy accurately.

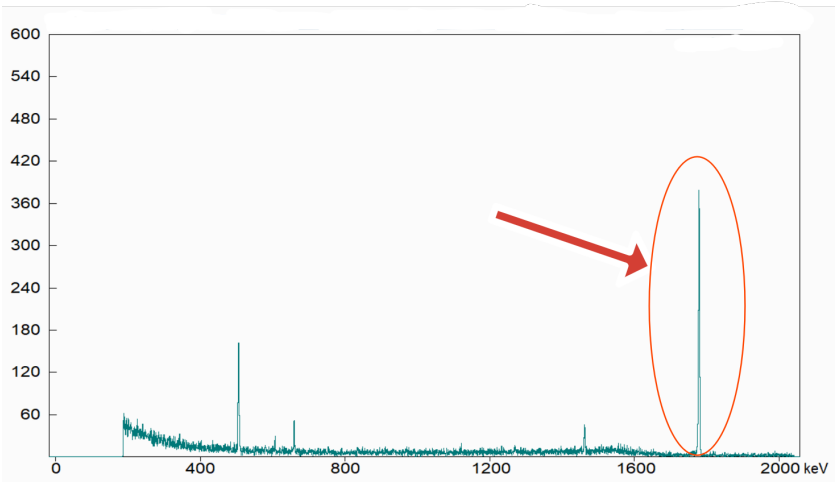

Figure 3.7: Typical machine calibration spectrum for an energy of $E_p = 992keV$. The arrow points out the gamma peak in interest.

Typically, the uncertainty of the beam energy (referred to as ripple) is determined via narrow resonances observed in (p, γ) reactions. In this study, the $^{27}Al(p,\gamma)^{18}Si$ reaction was employed, utilizing the resonance at $E_p = 991.89keV$ with Γ = 110 eV.

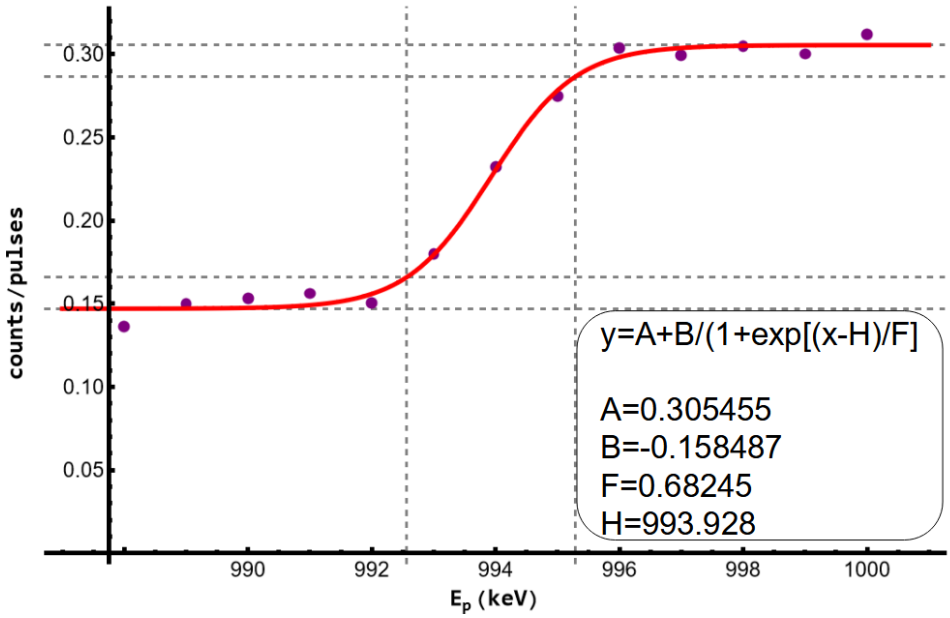

Figure 3.8: Machine calibration

To perform the calibration, a thick ^{27}Al target was mounted in the Faraday cup at the far end of the setup, with a Germanium detector placed directly behind the

target. The target was irradiated with a proton beam in the energy range of 988-1000 keV, with 1 keV steps to "scan" the resonance.

This reaction produces gamma particles with an energy of $E_\gamma = 1779keV$, pointed out by the arrow in the figure 3.7. The counts of this peak were calculated via integration using SpectrW, divided by the pulses (corresponding to the charge of the beam), and plotted against energy in figure 3.8. The function $y = A + B/(1 + exp[(x - H)/F]$ was used which displays a sigmoid curve. The midpoint of the rising edge corresponds to the beam energy, while the range from 12% to 88% of this edge indicates the energy error corresponding to the ripple. According to this, the offset is 2.05 keV, and the ripple is 2.7 keV. These deviations are considered stable throughout the entire energy range of the experiment.

3.4 Differential cross-section measurement

For the final calculations of the differential cross-section values, the 1.2 equation is used, as reminded below.

$$(\frac{d\sigma}{d\Omega})_{E,\theta} = \frac{N_{det}}{Q \cdot \Omega \cdot N_t} \tag{1.2}$$

These values are followed by their corresponding errors, calculated through error propagation according to equation 3.1

$$d\left(\frac{d\sigma}{d\Omega}\right) = \frac{d\sigma}{d\Omega} \cdot \sqrt{\left(\frac{dN_{det}}{N_{det}}\right)^2 + \left(\frac{d(Q \cdot \Omega)}{Q \cdot \Omega}\right)^2 + \left(\frac{dN_t}{N_t}\right)^2} \tag{3.1}$$

The energy of the particles just before the reaction must be accurately known, as the calculated differential cross sections need to correspond to the specific energy. Energy corrections are necessary both due to machine calibration, as described in Section 3.3, and because of energy loss from the particles interacting with the target material due to stopping power.

SIMNRA calculates the stopping power for each energy level in the middle of the target. For this calculation, the target's thickness must be known. The difference between the manufacturer-provided thickness and the experimentally determined thickness does not significantly impact the energy correction. Errors arise due to straggling, but rounding up these values results in a difference too small to affect the stopping power. The energy loss is consistently 2 keV across the entire energy range of the experiment. By combining the corrections from the machine calibration and the energy loss, the real energy of the beam occurs.

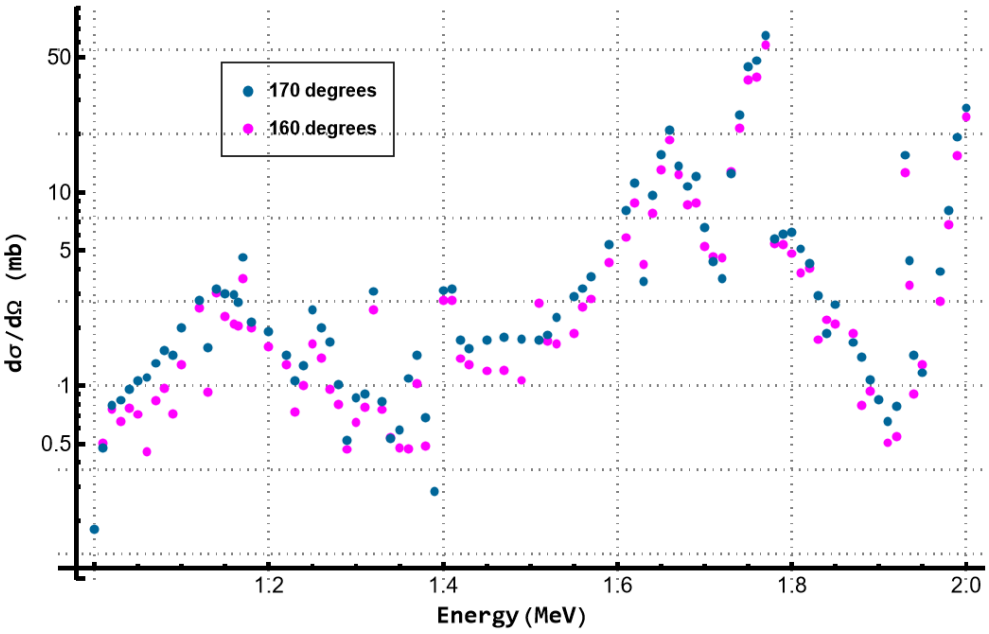

Figure 3.9: Differential cross section for the $^{18}O(p,\alpha)^{15}N$ in angular distribution

The results are depicted in figure 3.9 for angles 170^o and 160^o, using the thickness given by the manufacturer. A plethora of resonances are present, exhibiting wide variations in values. Some cross-section values are quite low, and only for energies higher than 1.7 MeV do they exceed 50 mb. There are no significant deviations between the two angles, except for a more erratic distribution at 160 degrees at low energies.

Because of the uncertainty regarding the target thickness, the differential cross sections are calculated for both the experimental target thickness (blue dots) and the one provided by the manufacturer (orange dots) presented in figures 3.10 and 3.11, separately for each angle.

For measurements at 170^o (figure 3.10), the results are also compared with the dataset from Amsel's first experiment(green dots) in 1964. Significant discrepancies were observed in the 1800-2000 keV region. It was discovered that the data for this region were incorrectly registered in the IBANDL library. Using a plot digitizer program, the correct data were extracted from the original paper [5] and used for comparison.

When comparing the two datasets from this work, a constant vertical shift between them is evident at both angles, indicating a systematic error attributed to the target thickness. At 170^o, a comparison with Amsel's dataset shows that the dataset using the manufacturer's target thickness is closer to Amsel's results. This raises concerns about the accuracy of the target thickness value, necessitating further investigation in the future.

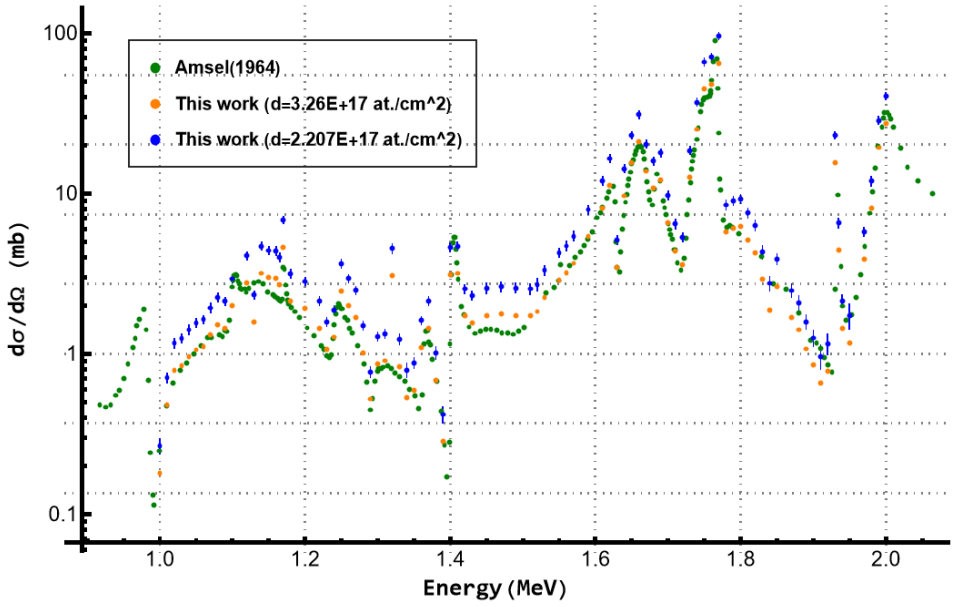

Figure 3.10: Differential cross section for the $^{18}O(p,\alpha)^{15}N$ at 170^o

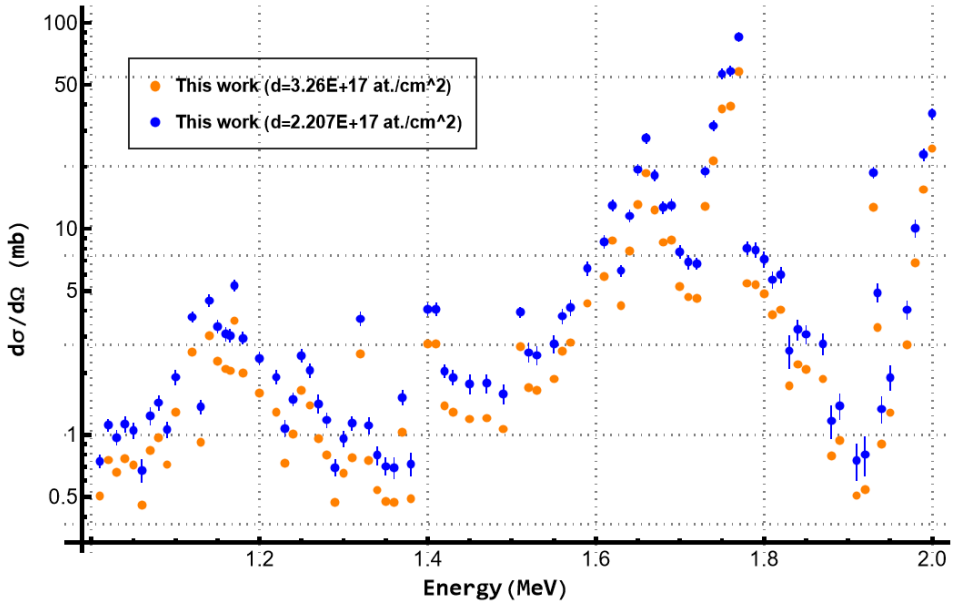

Figure 3.11: Differential cross section for the $^{18}O(p,\alpha)^{15}N$ at 160^o

Overall, the shape of the differential cross-section distribution from Amsel's experiment agrees with the findings of this study. However, a potential resonance was identified at 1320 keV, which does not appear in Amsel's data, requiring further examination.

Chapter 4

Conclusions and future perspectives

4.1 Conclusions

In this study, experimental measurements of reaction $^{18}O(p,\alpha)^{15}N$ cross-sections were conducted within the energy range of 1-2 MeV, at the detection angles of 170 and 160 degrees. A comparison was made with previously established data dating back to 1964, specifically for the 170^o angle. The current findings indicate a slight elevation in the measured differential cross-sections compared to the historical dataset. Nonetheless, the fundamental shape of the cross-section behavior remains consistent, except for 1320 keV where a possible resonance is recorded for the first time. Notably, a discrepancy between 1.8-2 MeV was subsequently traced back to a series of incorrect data entries within the IBANDL database. These coherent differential cross-section datasets are anticipated to facilitate the extension of the existing SigmaCalc evaluation of the $^{18}O(p,\alpha_0)$ reaction to higher energies in the near future. Additionally, experimental data were extended to new detection angles, with 160^o being a previously unmeasured angle for this reaction.

4.2 Future Perspectives

The primary issue to address is the target thickness. One alternative method involves using the resonance of $^{18}O(p,\alpha)15N$ reaction at 152 keV. This measurement was already conducted as mentioned in section 3.1.3, and the collected data are pending analysis. Hopefully, these results will help accurately determine the target thickness and resolve the issue of the vertical shift in the differential cross-section.

Another possible approach for calculating the thickness is the use of a heavy ion beam and the ToF-ERDA technique. As described in section 1.2.3, this technique allows for isotope identification and quantification.

If the final target thickness aligns with the manufacturer's specifications, the differential cross-section values for the $^{18}O(d,\alpha_0)$ and the $^{18}O(d,\alpha_0)$ reactions should be remeasured experimentally, as these values were used in our target thickness calculations. In the opposite scenario, the corresponding values for the $^{18}O(p,\alpha)$ reaction may not be accurate.

Additionally, measurements can be repeated using a more suitable target with a thinner backing to obtain data for additional detection angles.

Chapter 5

Appendix

5.1 Mylar test

In an effort to reduce the pile-up effect, the absorber foil technique was employed as the simplest method to stop unwanted particles [8]. A Mylar foil, a pinhole-free polyester film made from stretched polyethylene terephthalate, was placed in front of the detector to absorb excess particles. Various foil thicknesses were tested.

Unfortunately, the reduction in pile-up was minimal, and the significant energy straggling in the absorber foil led to poor depth resolution, negatively impacting the measurements.

5.2 Complimentary Data from Chopper

The chopper has one blade consisting of a thin layer of ^{197}Au on thick Aluminium as mentioned in section 2.4. Every ten seconds, when the blade intersects the proton beam for one second, it serves as a target for the $^{197}Au(p,p\gamma)^{197}Au$ reaction, which has a well-established differential cross-section. For this approach, the 1.2 equation is applied for both ^{18}O and ^{197}Au, as both reactions use the same beam, and therefore the same charge (Q). This method, combining the two equations from different reactions, is known as relative measurement described in this case by the following equation:

$$\left(\frac{d\sigma}{d\Omega}\right)_{^{18}O} = \left(\frac{d\sigma}{d\Omega}\right)_{^{197}Au} \cdot \frac{N_{det(O)}}{N_{det(Au)}} \cdot \frac{N_{t(Au)}}{N_{t(O)}} \tag{5.1}$$

The protons measured by the chopper's detector, were quantified using SPECTRW integration. Due to the limited reliability of the chopper data as discussed in section 2.4, the calculations were not performed analytically. Taking into consideration the detected particles from both reactions and the differential cross-section for ^{197}Au, a multiplication factor was applied to align them with the existing data. This approach was used to approximate and compare with existing data, as demonstrated in figure 5.1.

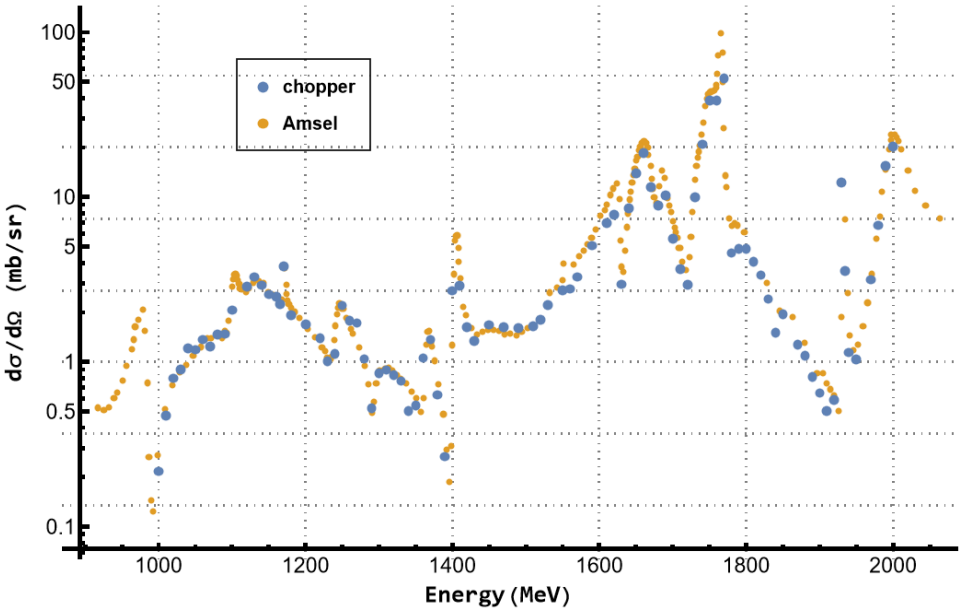

Figure 5.1: Differential cross section for the $^{18}O(p,\alpha)^{15}N$ at 160^o

The shape of the differential cross-section distribution closely resembles that of the existing data, which supports their validity.

Bibliography

[1] Cohen, D. D., Katsaros, A., & Carton, D. (1986). Some characteristics of the $^{18}O(p,\alpha_0)^{15}N$ reaction. Nuclear Instruments and Methods in Physics Research Section B: Beam Interactions with Materials and Atoms, 15(1-6), 555-558.

[2] J.R. Liu, Y.P. Li, Q.Y. Chen et al. (1998): "Depth resolution and dynamic range of $^{18}O(p,\alpha)^{15}N$ depth profiling", *Nuclear Instruments and Methods in Physics Research B, 136-138, p 1306-1311*

[3] Y. Kamemoto (1964): "Rapid non-destructive analysis of oxygen by neutron activation", Nature, 203, p 513-514

[4] N.S. Christensen et al. (1990): "Absolute calibration of the $^{18}O(p,\alpha_0)^{15}N$ nuclear reaction", Nuclear Instruments and Methods in Physics Research B, 51, p 97-101

[5] Georges Amsel(1964): "Spectroscopie par détecteurs à semiconducteur des réactions nucléaires O16 + d, O18 + p", Annales de Physique, Volume 13, (9), p 297 - 344

[6] Gurbich, A. F. (2016). SigmaCalc recent development and present status of the evaluated cross-sections for IBA. Nuclear Instruments and Methods in Physics Research Section B: Beam Interactions with Materials and Atoms, 371, 27-32. http://sigmacalc.iate.obninsk.ru/

[7] IBANDL database, IAEA, 2023: http://nds.iaea.org/ibandl/

[8] M. Nastasi, J.W. Mayer, Y. Wang (2014): "Ion Beam Analysis Fundamentals and Applications", CRC Press.

[9] K.S. Krane (1988): "Introductory nuclear physics", John Wiley & Sons.

[10] W.R. Leo(1994): "Techniques for Nuclear and Particle Physics Experiments, A How-to Approach", Springer-Verlag Berlin Heidelberg.

[11] G.F. Knoll (1979): "Radiation detection and measurement", John Wiley & Sons, Inc.

[12] G.R. Gilmore, (1995): "Practical Gamma-Ray Spectrometry", John Wiley & Sons, Ltd.

[13] R. Hellborg, H.J. Whitlow, Y. Zhang (2009), Ion Beams in Nanoscience and Technology, Springer Berlin, Heidelberg

[14] Wilson, R. G., Stevie, F. A., & Magee, C. W. (1989). "Secondary ion mass spectrometry: a practical handbook for depth profiling and bulk impurity analysis". New York, Surface and Interface Analysis, 17(4), 221–221.

[15] Thomson, J. J. (1910). LXXXIII. "Rays of positive electricity". The London, Edinburgh, and Dublin Philosophical Magazine and Journal of Science, 20(118), 752-767.

[16] D.S. McPhail, (2006). "Applications of secondary ion mass spectrometry (SIMS) in materials science". Journal of Materials Science, 41, 873-903.

[17] Aracheloff, C. (2020). "An in-situ study of the controlled oxidation of yttrium hydride thin films".

[18] Yasuda, K. (2020). "Time-of-flight erda for depth profiling of light elements", Quantum Beam Science, 4(4), p. 40. doi:10.3390/qubs4040040.

[19] H. A. Hill and J.M. Blair (1956): "Yields of the $^{18}O(p,\alpha)^{15}N$ and $^{18}O(p,n)^{18}F$ Reactions for protons of 800keV to 3500keV", Phys. Rev., 104, 198 DOI:https://doi.org/10.1103/PhysRev.104.198

[20] S. Amiel and M. Peisach (1963): "Oxygen-18 determination by counting delayed neutrons of Nitrogen-17", Analytical Chemistry, 35(3), 323-327.

[21] Amsel, Georges. and Samuel, David. (1967) 'Microanalysis of the stable isotopes of oxygen by means of nuclear reactions,' Analytical Chemistry, 39(14), pp. 1689–1698. https://doi.org/10.1021/ac50157a027.

[22] Battistig, G., Amsel, G., d'Artemare, E., & Vickridge, I. (1991). A very narrow resonance in 18O (p, α) 15N near 150 keV: Application to isotopic tracing: I. Resonance width measurement. Nuclear Instruments and Methods in Physics Research Section B: Beam Interactions with Materials and Atoms, 61(4), 369-376.

[23] Tempez, A.,et al. (2009). "18O/16O isotopic separation in anodic tantalum films by glow discharge time-of-flight mass spectrometry". Surface and Interface Analysis: An International Journal devoted to the development and application of techniques for the analysis of surfaces, interfaces, and thin films, 41(12-13), 966-973.

[24] Kottler, C., Döbeli, M., Glaus, F., & Suter, M. (2006). "A spectrometer for low energy heavy ion ERDA". Nuclear Instruments and Methods in Physics

Research Section B: Beam Interactions with Materials and Atoms, 248(1), 155-162.

[25] Giangrandi, S., Sajavaara, T., Brijs, B., Arstila, K., Vantomme, A., & Vandervorst, W. (2008). "Low-energy heavy-ion TOF-ERDA setup for quantitative depth profiling of thin films". Nuclear Instruments and Methods in Physics Research Section B: Beam Interactions with Materials and Atoms, 266(24), 5144-5150.

[26] Siketić, Z., Radović, I. B., & Jakšić, M. (2008). "Development of a time-of-flight spectrometer at the Ruder Bošković Institute in Zagreb". Nuclear Instruments and Methods in Physics Research Section B: Beam Interactions with Materials and Atoms, 266(8), 1328-1332.

[27] Jokinen, J., Keinonen, J., Tikkanen, P., Kuronen, A., Ahlgren, T., & Nordlund, K. (1996). "Comparison of TOF-ERDA and nuclear resonance reaction techniques for range profile measurements of keV energy implants". Nuclear Instruments and Methods in Physics Research Section B: Beam Interactions with Materials and Atoms, 119(4), 533-542.

[28] S. Harissopulos, M. Andrianis, M. Axiotis, et al., (2021): "The Tandem Accelerator Laboratory of NCSR "Demokritos": current status and perspectives.", The European Physical Journal Plus, 136, Issue 6, 617.

[29] Lagoyannis, A., Andrianis, M., Axiotis, M., Chatzispyroglou, P., Harissopulos, S., Laoutaris, A., Tsiamis, T. (2023). Recent upgrades at the Tandem Laboratory of NCSR "Demokritos". HNPS Advances in Nuclear Physics, 29, 33-37. doi: 10.12681/hnpsanp.5226

[30] Kalfas, C.A., Axiotis, M., Tsabaris, C. (2016). "SPECTRW: A software package for nuclear and atomic spectroscopy." Nuclear Instruments and Methods in Physics Research Section A: Accelerators Spectrometers Detectors and Associated Equipment. 830. 265-274. 10.1016/j.nima.2016.05.098.

[31] Mayer, M. (1999, June). SIMNRA, a simulation program for the analysis of NRA, RBS and ERDA. In AIP conference proceedings (Vol. 475, No. 1, pp. 541-544). American Institute of Physics.

[32] Karakaxi, A. (2024). Measurement and benchmarking of differential cross sections for deuteron-induced reactions in 13C, suitable for Nuclear Reaction Analysis (NRA). Bachelor thesis. http://dx.doi.org/10.26240/heal.ntua.27168